JOURNAL OF SPACECRAFT AND ROCKETS
Vol. 41, No. 4, July–August 2004

Three-Dimensional Magnetohydrodynamic Modeling of Plasma Jets in North Star Space Experiment

Nikolaos A. Gatsonis* and Michael DeMagistris†
Worcester Polytechnic Institute, Worcester, Massachusetts 01609
and
Robert E. Erlandson‡
Johns Hopkins University, Applied Physics Laboratory, Laurel, Maryland 20823

The Active Plasma Experiment (APEX) North Star mission involved the injection of two high-speed plasma jets. The first plasma jet with 30×10^{-3} kg of aluminum and kinetic energy of 6 MJ was injected at 360-km altitude nearly perpendicular to the ambient magnetic field. An air cloud was formed prior to the injection by releasing 12×10^{-3} kg of air. The jet, the air cloud, and the ambient constitute a partially ionized plasma modeled with a three-dimensional, single-fluid, unsteady, viscous, compressible magnetohydrodynamic formulation. The model equations are discretized with a finite volume implementation, and time integration is carried out with a multistep Runge–Kutta scheme. The simulation shows the deceleration of the jet, the induction of motion into the initially stationary ambient plasma and the formation of three-dimensional magntetohydrodynamic waves. The plasma density shows an enhancement over the ambient similar to Langmuir-probe measurements taken onboard the plasma diagnostics payload located approximately 468 m downstream the injection point. The simulation predicts the formation of a large diamagnetic cavity that almost excludes the ambient induction, in accordance with magnetometer measurements on the diagnostics payload. The numerical predictions of the components of the magnetic induction are also in good agreement with the measurements.

Nomenclature

$\boldsymbol{A}^{*\text{Face}}_{i,j,k}$	=	area vector of a face in a hexahedral cell with vertex (i, j, k)
$\boldsymbol{B}$	=	magnetic induction, nT
$\boldsymbol{B}_a$	=	ambient magnetic induction, nT
c_v, c_p	=	specific heat at constant volume and constant pressure, J/K · kg
$\boldsymbol{D}$	=	dissipation operator
$\boldsymbol{E}$	=	electric field, V/m
E_J	=	total kinetic energy of the aluminum plasma jet, MJ
e	=	electron charge, 1.602×10^{-19} C
e_i	=	internal energy per unit mass, J/kg
$\bar{\bar{F}}$	=	flux tensor
$\boldsymbol{f}$	=	flux vector in x direction
$\boldsymbol{g}$	=	flux vector in y direction
$\boldsymbol{h}$	=	flux vector in z direction
$\boldsymbol{J}$	=	total current density vector, A/m^2
$\boldsymbol{j}$	=	conduction current density vector, A/m^2
k	=	Boltzmann's constant, 1.381×10^{-23} J/K
L	=	length, m
L_J	=	length of the aluminum plasma jet at initialization, m
M_c	=	total mass of air cloud, kg
M_{ec}	=	Mach number at the exit of the air-cloud nozzle
M_J	=	total mass of the aluminum plasma jet, kg
M_{M0}	=	magnetic Mach number (Alfvén number)
M_0	=	Mach number
m_s	=	mass of particle species s, kg
$\boldsymbol{n}$	=	unit normal vector
n_s	=	number density of species s, m^{-3}
P_M	=	magnetic pressure, Pa
Pr	=	Prandtl number
p	=	pressure, Pa
Q_c	=	number of released air-cloud particles
$\boldsymbol{q}$	=	heat addition per unit mass, J/kg
R	=	gas constant, J/K · kg
$\boldsymbol{R}$	=	summation of right-hand side vector
R_J	=	radius of the aluminum plasma jet at initialization, m
Re_{M0}	=	reference magnetic Reynold's number
Re_0	=	reference Reynold's number
S	=	ion slip factor
$(\boldsymbol{S}^*_{\max})_{i,j,k}$	=	local vector sum of the maximum projected areas in a hexahedral cell with vertex (i, j, k)
T	=	temperature, K
$\bar{\bar{T}}$	=	viscous stress tensor, Pa
T_{ec}	=	temperature at exit of the air cloud nozzle, K
T_s	=	temperature of species s, K
T_{sc}	=	source temperature of the air cloud, K
t	=	time, s
$\boldsymbol{U}$	=	state vector of conservative variables
$\boldsymbol{U}_s$	=	diffusion velocity of species, m/s
u, v, w	=	Cartesian components of velocity vector, m/s
u_{ec}	=	velocity at exit of the air-cloud nozzle, m/s
u_{sc}	=	source velocity of the air cloud, m/s
$\boldsymbol{V}$	=	mean mass velocity, m/s
V_A	=	Alfvén speed, m/s
$\boldsymbol{V}_s$	=	mean velocity of species s, m/s
$\boldsymbol{W}$	=	state vector of primitive variables
W_{sc}	=	molecular speed over most probable thermal speed
x, y, z	=	Cartesian components of position vector, m
Z	=	charge number
γ	=	ratio of specific heats (c_v/c_p)
ΔB_i	=	perturbation of the ith component of the magnetic induction, T

Received 26 October 2001; revision received 5 June 2003; accepted for publication 30 August 2003.

*Associate Professor, Mechanical Engineering Department, 100 Institute Road; gatsonis@wpi.edu. Senior Member AIAA.

†Graduate Research Assistant; currently Research Scientist, Combustion Research and Flow Technology, 461 South Tenth Street, Quakertown, PA 18951; strates@craft-tech.com. Member AIAA.

‡Senior Professional Staff, Space Department, Johns Hopkins Road; erlandson@jhuapl.edu.

Δt = time step, s
κ = coefficient of thermal conductivity, W/m · K
μ = absolute magnetic permeability for plasma, $4\pi \times 10^{-7}$ H/m
μ_v = coefficient of viscosity, kg/m · s
μ_0 = magnetic permeability constant for free space, $4\pi \times 10^{-7}$ H/m
$\bar{\nu}_{st}$ = average momentum-transfer collision frequency between species s and t, s^{-1}
ρ = mass density, kg/m^3
ρ_C = charge density, C/m^3
ρ_s = mass density of species s, kg/m^3
σ = electrical conductivity, S/m
τ_0 = time of operation of the air-cloud source, s
$\Omega_{i(e)}$ = gyrofrequency of ion or electron, Hz
$\Omega_{i,j,k}$ = control volume, m^3
ω_p = plasma frequency, Hz

Subscripts and Superscripts

C_a = macroscopic variable (property) C ambient neutrals
C_a^+ = macroscopic variable (property) C of ambient ions
C_a^e = macroscopic variable (property) C of ambient electrons
C_c = macroscopic variable (property) C of air-cloud neutrals
C_J = total macroscopic variable (property) C of plasma jet
C_j^e = macroscopic variable (property) C of jet electrons
C_j^+ = macroscopic variable (property) C of jet aluminum ions
c = air-cloud neutral
e = electron
H = heavy plasma species
i = ion
0 = characteristic value used in nondimensionalization of variables

Introduction

DURING the Active Plasma Experiment (APEX) North Star mission, two high-speed aluminum plasma jets were injected in the ionosphere from the explosive-type generator (ETG) payloads carried onboard a suborbital rocket. The ETG-1 plasma jet was injected at an altitude of 360 km and the ETG-2 plasma jet at an altitude of 280 km during the descending part of the trajectory. Instruments were carried onboard the plasma diagnostic payload (PDP) and the optical sensor payload deployed from the suborbital rocket prior to the jet injection. The instrument payloads are shown in Fig. 1 at the time of the ETG-1 plasma-jet injection and measured the plasma density, magnetic perturbations, electric fields, and the optical environment associated with the plasma jets.[1]

High-speed plasma jets with physical characteristics similar to the APEX jets can be a result of onboard electric propulsion thrusters, the release of neutrals and/or plasma from spacecraft subsystems, or active release experiments. As the APEX measurements demonstrate, high-speed plasma jets result in an induced environment that includes density, electric and magnetic field perturbations, as well as optical emissions.[1] The effects of the plume-induced environment on spacecraft has been an active area of investigation. The majority of plasma plume/spacecraft interaction studies has been focused in near-field effects.[2] However, the APEX measurements show that the induced environment of a high-speed plasma jet includes perturbations at scales that are much larger than a typical spacecraft. The increased utilization of onboard electric propulsion devices as well as the possibilities for spacecraft formation flying make the APEX findings and studies of plasma-jet/ambient interactions very important.

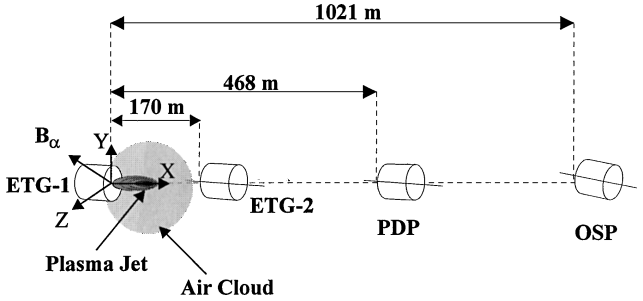

Fig. 1 Schematic of the APEX ETG-1 plasma-jet experiment. Distances shown are at the time of the ETG-1 plasma-jet injection.

The present study involves the modeling and numerical simulation of the ETG-1 aluminum plasma jet that was injected into an air cloud formed 0.2 s prior to the ETG detonation. The model that describes the aluminum plasma jet, the air cloud, and the ambient plasma is based on a set of three-dimensional, single-fluid, compressible, viscous, magnetohydrodynamic (MHD) equations or magnetogasdynamic (MGD) equations. The single-fluid description of an expanding plasma and the associated wave structure using the MGD equations has been compared favorably with kinetic-based solutions.[3,4] Multifluid but steady-state formulations have also been utilized in modeling high-speed aluminum plasma jets released during the Fluxus experiments[5] as well as in modeling plasma clouds released from the shuttle.[6,7] The numerical solution of the MGD equations presented in the current study is based on a finite volume spatial discretization method (FVM) and a time-accurate integration using a multistep Runge–Kutta scheme. The MGD-FVM has been applied to spherically expanding plasmas, but the physical model of our earlier work[8] has been further expanded to include initial conditions for the air cloud present during the ETG-1 plasma-jet injection. In addition, in the present work a multigrid layering method is implemented in order to address the largely dissimilar length scales encountered during the expansion of a plasma jet.

The model equations and numerical methodology are presented first followed by the development of initial conditions for ambient, the air cloud, and the ETG-1 plasma jet. Simulation results are discussed, and the predicted plasma density and magnetic induction perturbations are compared with measurements obtained onboard the PDP payload.

Viscous Magnetohydronamic Model

The model represents the expansion of a plasma jet generated at a specified altitude in an ambient magnetic field $\boldsymbol{B}_a$ shown schematically in Fig. 1. The plasma consists of s types of particles (or species) that include the jet ion species j^+, jet electrons j^e, ambient (or background) neutrals a, ambient ions a^+, ambient electrons a^e, and air-cloud neutrals c. Number density, temperature, and mean velocity of a species s with mass m_s charge $q_s = Z_s e$ are given by n_s, T_s, $\boldsymbol{V}_s$, respectively. The macroscopic, single-fluid plasma variables (or properties) of the plasma jet-background are given by the mass density

$$\rho = \sum_s n_s m_s \tag{1}$$

the charge density

$$\rho_C = \sum_s n_s q_s \tag{2}$$

and the mean mass velocity of the fluid as a whole is

$$\boldsymbol{V} = \sum_s \rho_s \boldsymbol{V}_s \Big/ \rho \tag{3}$$

The total current density is the sum of convection and conduction currents, respectively,

$$\boldsymbol{J} = \sum_s n_s e_s \boldsymbol{V}_s = \rho_c \boldsymbol{V} + \sum_s n_s e_s \boldsymbol{U}_s = \rho_c \boldsymbol{V} + \boldsymbol{j} \tag{4}$$

where the species diffusion velocity is

$$\boldsymbol{U}_s = \boldsymbol{V}_s - \boldsymbol{V} \tag{5}$$

The derivation of a set of single-fluid MHD (or MGD) equations begins with the continuity, momentum, and energy equation for each species in the plasma supplemented with Maxwell's equations.[9] Several simplifications outlined subsequently lead to the MGD equations used in this work.

The plasma is considered to be charge neutral

$$\rho_C \gg e n_e \tag{6}$$

so that $n_e \approx n_i$. The characteristic time for macroscopic change in the flow satisfies

$$\tau_c \gg \bar{\nu}_{\mathrm{eH}} \Big/ \omega_p^2 \tag{7}$$

$$\tau_c \gg \bar{\nu}_{\mathrm{eH}}^{-1} \tag{8}$$

$$\tau_c \gg \bar{\nu}_{\mathrm{in}}^{-1} \tag{9}$$

where $\bar{\nu}_{\mathrm{eH}} = \bar{\nu}_{ei} + \bar{\nu}_{en}$ is the average momentum-transfer collision frequency of electrons with heavy particles (ions and neutrals) and $\omega_p = (n_e e^2/\varepsilon_0 m_e)^{1/2}$ is the plasma frequency. The plasma is also considered to be collision dominated so that for $s \equiv e, i$

$$\beta_s = (eB/m_s \bar{\nu}_{\mathrm{sH}}) \ll 1 \tag{10}$$

and the ion-slip factor satisfies

$$S = (\rho_n/\rho)^2 \beta_e \beta_i \ll 1 \tag{11}$$

For a partially ionized plasma under assumptions given by Eqs. (6–11) or for plasma where $\tau_c \gg \tau_{ci}$ (where τ_{ci} is the ion Larmor time), the generalized Ohm's law that can obtained from manipulation of the single-species momentum equations[9] reduces to

$$\boldsymbol{j} = \sigma[\boldsymbol{E} + \boldsymbol{V} \times \boldsymbol{B}] = \sigma \boldsymbol{E}' \tag{12}$$

In Eq. (12), $\boldsymbol{E}$ is the electric field in the inertial reference frame, $\boldsymbol{E}'$ in the frame moving with the mean fluid velocity $\boldsymbol{V}$, and the electrical conductivity is

$$\sigma = n_e e^2 \Big/ m_e \bar{\nu}_{\mathrm{eH}} \tag{13}$$

Using Ohm's law equation (12) and scaling arguments, the convection current can be neglected in comparison to conduction current in Eq. (4), leading to

$$\boldsymbol{j} = \boldsymbol{J} \tag{14}$$

Using the assumption in Eq. (7) and Ohm's law equation (12), the displacement current can be neglected in comparison to conduction current so that the Ampere–Maxwell equation becomes

$$\nabla \times \boldsymbol{B}/\mu = \boldsymbol{j} \tag{15}$$

Faraday's law is

$$\nabla \times \boldsymbol{E} = -\frac{\partial \boldsymbol{B}}{\partial t} \tag{16}$$

Using the assumptions (8–11) just outlined, Ohm's law equation (12), and Maxwell equations (15) and (16), the multispecies plasma in the present work is described with the following system of MGD equations:

$$\frac{\partial \rho}{\partial t} + \nabla \cdot (\rho \boldsymbol{V}) = 0 \tag{17}$$

$$\frac{\partial}{\partial t}(\rho \boldsymbol{V}) + \nabla \cdot (\rho \boldsymbol{V}\boldsymbol{V}) + \nabla p - \nabla \cdot \bar{\bar{\boldsymbol{T}}} + \frac{1}{\mu_0}[\nabla(\boldsymbol{B} \cdot \boldsymbol{B}) - (\boldsymbol{B} \cdot \nabla)\boldsymbol{B}] = 0 \tag{18}$$

$$\frac{\partial}{\partial t}\left(\frac{p}{\gamma - 1} + \rho \frac{\boldsymbol{V}^2}{2} + \frac{B^2}{2\mu}\right) + \nabla \cdot \left(\frac{\gamma}{\gamma - 1} p \boldsymbol{V}\right) - \nabla \cdot (\bar{\bar{\boldsymbol{T}}} \cdot \boldsymbol{V}) + \nabla \cdot \boldsymbol{q} - \frac{1}{\mu} \nabla \cdot \left[\left(\frac{\nabla \times \boldsymbol{B}}{\mu\sigma} - \boldsymbol{V} \times \boldsymbol{B}\right) \times \boldsymbol{B}\right] = 0 \tag{19}$$

$$\frac{\partial \boldsymbol{B}}{\partial t} + \frac{1}{\sigma \mu_0} \nabla^2 \boldsymbol{B} - \nabla \cdot (\boldsymbol{B} \cdot \boldsymbol{V} - \boldsymbol{V} \cdot \boldsymbol{B}) = 0 \tag{20}$$

The viscous stress tensor appearing in the momentum equation (18) is given by

$$\bar{\bar{\boldsymbol{T}}} = \mu_v \left[\left(\frac{\partial V_i}{\partial x_j} + \frac{\partial V_j}{\partial x_i}\right) - \frac{2}{3} \frac{\partial V_k}{\partial x_k} \delta_{ij}\right]$$

$$\delta_{ij} = \begin{cases} 0 & \text{if} \quad i \neq j \\ 1 & \text{if} \quad i = j \end{cases} \tag{21}$$

with the coefficient of viscosity given by

$$\mu_v = \frac{\sqrt{m_i}(kT_i)^{\frac{5}{2}}}{Z^4 e^4 \ell_n \Lambda} \tag{22}$$

where the Coulomb logarithm is[9] $\ell_n \Lambda = \ell_n(1.24 \times 10^{24} T^{3/2} n_e^{-1/2})$. The plasma is modeled as a perfect gas with pressure:

$$p = \sum_s \rho_s R T_s = \rho R T \tag{23}$$

and internal energy per unit mass

$$e_i = c_v T = p/\rho(\gamma - 1) \tag{24}$$

In Eqs. (23) and (24) R is the gas constant and c_v is related to the specific heat at constant pressure by

$$\gamma = c_p/c_v, \qquad c_p = \gamma R/(\gamma - 1) \tag{25}$$

The heat transfer by conduction per unit mass in Eq. (19) is given by Fourier's law

$$\boldsymbol{q} = -\kappa \nabla T \tag{26}$$

where the thermal conductivity κ is

$$\kappa = 3.203 \frac{n_e k^2 T_e}{m_e \bar{\nu}_{\mathrm{eH}}} = c_p \mu_v / Pr \tag{27}$$

In the energy equation (19) the term

$$P_M = B^2/2\mu \tag{28}$$

is defined as the magnetic pressure, where $\mu = \mu_0$ is the absolute permeability of the plasma. The system of Eqs. (17–20) is supplemented by the divergence-free condition of the magnetic induction expressed by

$$\nabla \cdot \boldsymbol{B} = 0 \tag{29}$$

The preceding is not an additional equation but an initial condition that needs to be satisfied at all times throughout the domain.

The system of Eqs. (17–20) is nondimensionalized and written in a conservative flux-vector form as

$$\frac{\partial \boldsymbol{U}^*}{\partial t^*} + \nabla^* \cdot \bar{\boldsymbol{F}}^* = 0 \tag{30}$$

where the nondimensional state vector is

$$\boldsymbol{U}^* = \left[\rho^*, \rho^* u^*, \rho^* v^*, \rho^* w^*, \frac{p^*}{(\gamma - 1)} + \frac{\rho(u^{*2} + v^{*2} + w^{*2})}{2} + \frac{\left(B_x^{*2} + B_y^{*2} + B_z^{*2}\right)}{2\mu^* M_{M0}^2}, B_x^*, B_y^*, B_z^*\right]^T \tag{31}$$

The (8×3) tensor $\bar{\boldsymbol{F}}^*$ in Eq. (30) is given in Cartesian coordinates by

$$\bar{\boldsymbol{F}}^* = \left(\boldsymbol{f}_I^* + \boldsymbol{f}_V^* + \boldsymbol{f}_{M1}^* + \boldsymbol{f}_{M2}^*\right)\hat{\boldsymbol{x}} + \left(\boldsymbol{g}_I^* + \boldsymbol{g}_V^* + \boldsymbol{g}_{M1}^* + \boldsymbol{g}_{M2}^*\right)\hat{\boldsymbol{y}} + \left(\boldsymbol{h}_I^* + \boldsymbol{h}_V^* + \boldsymbol{h}_{M1}^* + \boldsymbol{h}_{M2}^*\right)\hat{\boldsymbol{z}} \tag{32}$$

The nondimensional (8×1) flux vectors in Eq. (32) account for contributions from the inviscid (I), viscous (V), and magnetic ($M1$ and $M2$) terms. The flux vectors in the $\hat{\boldsymbol{x}}$ direction are given by

$$\boldsymbol{f}_I^* = \left[\rho^* u^*,\ \rho^* u^{*2} + p^*,\ \rho^* u^* v^*,\ \rho^* u^* w^*,\ u^* \frac{\gamma p^*}{(\gamma - 1)} + \frac{\rho^* u^* (u^{*2} + v^{*2} + w^{*2})}{2},\ 0,\ 0,\ 0\right]^T \tag{33}$$

$$\boldsymbol{f}_V^* = \left[0,\ -\frac{2\mu_v^*}{3Re_0}\left(2\frac{\partial u^*}{\partial x^*} - \frac{\partial v^*}{\partial y^*} - \frac{\partial w^*}{\partial z^*}\right),\ -\frac{\mu_v^*}{Re_0}\left(\frac{\partial u^*}{\partial y^*} + \frac{\partial v^*}{\partial x^*}\right),\ -\frac{\mu_v^*}{Re_0}\left(\frac{\partial u^*}{\partial z^*} + \frac{\partial w^*}{\partial x^*}\right),\ -\frac{2\mu_v^*}{3Re_0}\left(2\frac{\partial u^*}{\partial x^*} - \frac{\partial v^*}{\partial y^*} - \frac{\partial w^*}{\partial z^*}\right)u^* - \frac{\mu_v^*}{Re_0}\left(\frac{\partial u^*}{\partial y^*} + \frac{\partial v^*}{\partial x^*}\right)v^* - \frac{\mu_v^*}{Re_0}\left(\frac{\partial u^*}{\partial z^*} + \frac{\partial w^*}{\partial x^*}\right)w^* + \frac{\mu_v^*}{(\gamma - 1)M_0^2 Re_0 Pr}\frac{\partial T^*}{\partial x^*},\ 0,\ 0,\ 0\right]^T \tag{34}$$

$$\boldsymbol{f}_{M1}^* = \left[0,\ -\frac{1}{2\mu^* M_{M0}^2}\left(B_x^{*2} - B_y^{*2} - B_z^{*2}\right),\ -\frac{1}{\mu^* M_{M0}^2}B_x^* B_y^*,\ -\frac{1}{\mu^* M_{M0}^2}B_x^* B_z^*,\ \frac{\left[u^*\left(B_x^{*2} + B_y^{*2} + B_z^{*2}\right) - B_x^*\left(u^* B_x^* + v^* B_y^* + w^* B_z^*\right)\right]}{2\mu^* M_{M0}^2},\ 0,\ -v^* B_x^* + u^* B_y^*,\ -w^* B_x^* + u^* B_z^*\right]^T \tag{35}$$

$$\boldsymbol{f}_{M2}^* = \left[0,\ 0,\ 0,\ 0,\ \frac{1}{Re_{M0} M_{M0}^2 \mu^{*2}\sigma^*}\left[B_y^*\left(\frac{\partial B_x^*}{\partial y^*} - \frac{\partial B_y^*}{\partial x^*}\right) + B_z^*\left(\frac{\partial B_x^*}{\partial z^*} - \frac{\partial B_z^*}{\partial x^*}\right)\right],\ 0,\ \frac{1}{Re_{M0}\mu^*\sigma^*}\left(\frac{\partial B_y^*}{\partial x^*} - \frac{\partial B_x^*}{\partial y^*}\right),\ -\frac{1}{Re_{M0}\mu^*\sigma^*}\left(\frac{\partial B_x^*}{\partial z^*} - \frac{\partial B_z^*}{\partial x^*}\right)\right]^T \tag{36}$$

Similar expressions hold for the flux vectors in the $\hat{\boldsymbol{y}}$ and $\hat{\boldsymbol{z}}$ directions $\boldsymbol{g}_V^*$, $\boldsymbol{h}_V^*$, $\boldsymbol{g}_{M1}^*$, $\boldsymbol{g}_{M2}^*$, and $\boldsymbol{h}_{M1}^*$, $\boldsymbol{h}_{M2}^*$ and are given in the Appendix. The nondimensional variables in Eqs. (31) and (33–36) are $x^* = x/L_0$, $y^* = y/L_0$, $z^* = z/L_0$, $t^* = tV_0/L_0$, where $V_0 = \sqrt{(\gamma p_0/\rho_0)}$, $u^* = u/V_0$, $v^* = v/V_0$, $w^* = w/V_0$, $p^* = p/\rho_0 V_0^2$, $B_x^* = B_x/B_0$, $B_y^* = B_y/B_0$, $B_z^* = B_z/B_0$, $\kappa^* = \kappa/\kappa_0 = \mu_v/\mu_{v0} = \mu_v^*$, $\mu^* = \mu/\mu_0 = 1$, and $\sigma^* = \sigma/\sigma_0$. The dimensionless parameters are the Mach number $M_0 = V_0/\sqrt{(\gamma R T_0)}$, the Reynolds number $Re_0 = \rho_0 V_0 L_0/\mu_{v0}$ the magnetic Reynolds number $Re_{M0} = \sigma_0\mu_0 V_0 L_0$, the magnetic Mach or Alfvén number $M_{M0} = V_0/V_{A0}$, which is the ratio of the fluid speed to Alfvén speed $V_{A0} = \sqrt{(B_0^2/\mu_0\rho_0)}$, and the Prandlt number $Pr = c_p\mu_v/\kappa$.

Numerical Methodology

The system expressed by Eq. (30) is solved with a magnetogasdynamics finite volume method (MGD-FVM) in a domain that is discretized with hexahedral control volumes.[10,11] Integrating over a control volume Ω^* with a surface area $\boldsymbol{A}^* = A^*\hat{\boldsymbol{n}}$ Eq. (30) becomes

$$\frac{\partial}{\partial t^*}\iiint_{\Omega^*} \boldsymbol{U}^*\,\mathrm{d}V^* + \oiint_{A^*} \bar{\boldsymbol{F}}^* \cdot \mathrm{d}\boldsymbol{A}^* = 0 \tag{37}$$

The integrations are carried out over the east, west, north, south, back, and front faces of the hexahedral control-volume cells to form the following system of semidiscrete equations:

$$\frac{\mathrm{d}\boldsymbol{U}_{i,j,k}^*}{\mathrm{d}t^*} = -\frac{1}{\Omega_{i,j,k}^*}\sum_{\text{Face}} \bar{\boldsymbol{F}}_{i,j,k}^{*\text{Face}} \cdot \boldsymbol{A}_{i,j,k}^{*\text{Face}} = \boldsymbol{R}_{i,j,k}^* \tag{38}$$

where Ω_{ijk}^* is the volume of the cell with vertex at (i, j, k), and $\boldsymbol{A}_{i,j,k}^{*\text{Face}}$ is the area vector of the each face. A dissipation operator $\boldsymbol{D}_{ijk}$ is supplied to the right-hand-side vector $\boldsymbol{R}_{ijk}$ in order to reduce numerical oscillations associated with centrally discretized second-order schemes. The right-hand side of Eq. (38) becomes

$$\boldsymbol{R}_{i,j,k}^{*(AV)} = \boldsymbol{R}_{i,j,k}^* + \boldsymbol{D}_{i,j,k} \tag{39}$$

The dissipation operator $\boldsymbol{D}_{i,j,k}^G$ follows the gasdynamic formulation[11] but uses the normalized magnetic pressure $p_M^* = p_M/p_{M0} = B^2/B_0^2$ and gasdynamic pressure p^* to evaluate the required coefficients.[8,12] The system of semidiscrete ordinary differential equations in Eq. (38) is integrated using the four-step Runge–Kutta scheme[10,11] expressed as

$$\boldsymbol{U}^{*(m)} = \boldsymbol{U}^{*(n)} - \alpha_m \Delta t^* \boldsymbol{R}^{*(AV)} \boldsymbol{U}^{*(m-1)}, \qquad m = 1, 2, 3, 4$$
$$\boldsymbol{U}^{*(n+1)} = \boldsymbol{U}^{*(4)} \tag{40}$$

where $\boldsymbol{U}^{*(n)}$ is the state vector at time level n and $\alpha_1 = 0.25$, $\alpha_2 = 0.333$, $\alpha_3 = 0.5$, and $\alpha_4 = 1$. The global time step used is the minimum found in the domain, given by

$$\Delta t^* = \min\left\{\text{CFL}\left[\Omega_{i,j,k}^* \Big/ \left(\left|\boldsymbol{u}^* \cdot \boldsymbol{S}_{\max}^*\right| + V_A^* \left|\boldsymbol{S}_{\max}^*\right|\right)\right]_{ijk}\right\} \tag{41}$$

The local time step is a function of the Courant–Friedrichs–Lewy (CFL) number, the local super-Alfvénic characteristic wave $(u^* + V_A^*)$, the local vector sum of the maximum projected areas $\boldsymbol{S}_{\max}^*$, and the local cell volume Ω_{ijk}^*. The CFL number lies in the range $0.001 \le \text{CFL} \le 0.1$.

The state vector $\boldsymbol{U}^*$ in Eq. (31) is applied at the center of a finite volume cell and contains all the necessary primitive variables to calculate the flux vectors $\boldsymbol{f}_I^*, \boldsymbol{g}_I^*, \boldsymbol{h}_I^*, \boldsymbol{f}_{M1}^*, \boldsymbol{g}_{M1}^*$, and $\boldsymbol{h}_{M1}^*$. Consequently, the inviscid gasdynamic and first-magnetic vectors are located at the cell center and calculated directly from the state vector $\boldsymbol{U}^*$. To find inviscid fluxes at the cell interfaces, we use the procedure of averaging the adjacent cell-centered fluxes.[10] The viscous gasdynamic and second-magnetic flux vectors $\boldsymbol{f}_V^*, \boldsymbol{g}_V^*, \boldsymbol{h}_V^*, \boldsymbol{f}_{M2}^*, \boldsymbol{g}_{M2}^*, \boldsymbol{h}_{M2}^*$ are composed of the first-order derivative terms and are calculated on the cell interfaces. The first-order derivative terms are calculated with a three-dimensional extension of a method originally developed in Ref. 11 for the two-dimensional Navier–Stokes equations. All gradient terms such as velocity, temperature, magnetic induction gradients are calculated at the cell interfaces. [13]

The numerical solution of the MGD equations requires also the preservation of a divergence-free magnetic induction condition. It is well known that numerical violation of Eq. (29) can lead to spurious oscillations.[14] In our MGD-FVM implementation the divergence-free condition is verified by the numerical evaluation of $\nabla \cdot \boldsymbol{B}$. The procedure has been applied to spherically expanding plasmas[8] and compared to successfully to analytical solutions.[12]

Initial Conditions and Simulations

The ETG-1 plasma jet injection occurred at an altitude of 360 km while the PDP payload was located at a distance of approximately 468 m as shown in Fig. 1. During the experiment the PDP was moving with a speed of approximately 2000 m/s. Figure 2 shows the number density measured by the PDP Langmuir probe and the

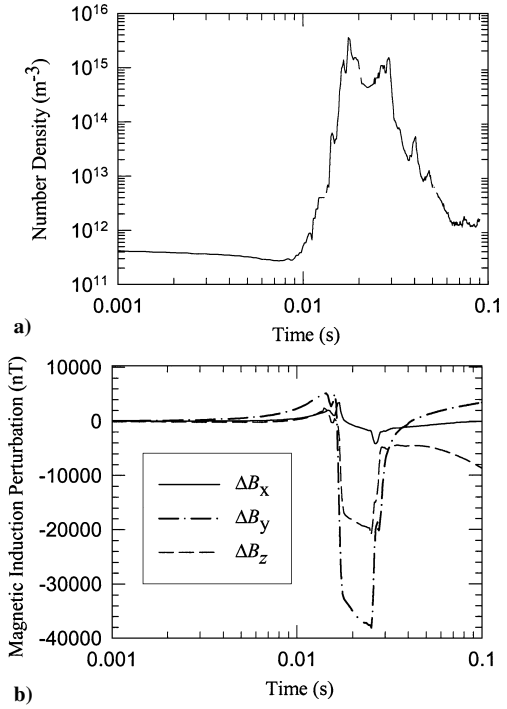

Fig. 2 Measurements onboard the PDP payload during the APEX ETG-1 plasma jet experiment: a) number density from a spherical Langmuir probe and b) magnetic field perturbations from the fluxgate magnetometer. Time is measured with respect to the ETG-1 plasma-jet injection with the jet velocity toward $\hat{x}$ perpendicular to $\boldsymbol{B}_a = (B_{xa} = 0, B_{ya} = 40{,}000, B_{za} = 22{,}000)$ nT.

magnetic induction perturbations measured by the PDP fluxgate magnetometer.[15] The $\boldsymbol{B}$-field components shown in Fig. 2 follow the coordinate system adapted in Fig. 1. Figure 2 indicates that the density and magnetic induction perturbations reached the PDP sensors at about $t = 8 \times 10^{-3}$ s after the ETG-1 injection and lasted for up to approximately $t = 35 \times 10^{-3}$ s. During the observation period, the PDP motion resulted in a displacement of about 70 m from its original position. Prior to the detonation of the ETG-1, an air cloud was formed by ejecting a total mass of 12×10^{-3} kg of condensed air over a period of about 0.2 s.

The ETG-1 simulation follows the evolution of the aluminum plasma jet from initialization at $t = 0$ s up to $t = 27 \times 10^{-3}$ s time at which the front of the jet has reached at a distance of 900 m downstream of the injection point well past the PDP position. Initial conditions for the simulation of the ETG-1 experiment involve the specification of plasma parameters for the ambient plasma, the air cloud, and the aluminum plasma jet that are described next. These initial conditions provide the fluid variables (or properties) of the single-fluid plasma at the time of the ETG-1 detonation, specifically, the mass density through Eq. (1):

$$\rho(\boldsymbol{r}, t=0) = \left[\rho_a^+(\boldsymbol{r}, t=0) + \rho_a^e(\boldsymbol{r}, t=0) + \rho_a(\boldsymbol{r}, t=0)\right] + \left[\rho_j^+(\boldsymbol{r}, t=0) + \rho_j^e(\boldsymbol{r}, t=0)\right] + \rho_c(\boldsymbol{r}, t=0) \tag{42}$$

the mean flow velocity through Eq. (3):

$$\boldsymbol{V}(\boldsymbol{r}, t=0) = \left[\rho_a^+(\boldsymbol{r}, t=0)\boldsymbol{V}_a^+(\boldsymbol{r}, t=0) + \rho_a^e(\boldsymbol{r}, t=0)\boldsymbol{V}_a^e(\boldsymbol{r}, t=0) + \rho_a(\boldsymbol{r}, t=0)\boldsymbol{V}_a(\boldsymbol{r}, t=0)\right]/\rho \times \left[\rho_j^+(\boldsymbol{r}, t=0)\boldsymbol{V}_j^+(\boldsymbol{r}, t=0) + \rho_j^e(\boldsymbol{r}, t=0)\boldsymbol{V}_j^e(\boldsymbol{r}, t=0)\right]/\rho + [\rho_c(\boldsymbol{r}, t=0)\boldsymbol{V}_c(\boldsymbol{r}, t=0)]/\rho \tag{43}$$

and the pressure through Eq. (23):

$$p(\boldsymbol{r}, t=0) = \left[p_a^+(\boldsymbol{r}, t=0) + p_a^e(\boldsymbol{r}, t=0) + p_a(\boldsymbol{r}, t=0)\right] \times \left[p_j^+(\boldsymbol{r}, t=0) + p_j^e(\boldsymbol{r}, t=0)\right] + p_c(\boldsymbol{r}, t=0) \tag{44}$$

Ambient Plasma Initial Conditions

We assume that the ambient plasma is uniform, stationary, and is composed of oxygen ions, oxygen neutrals and electrons. The ambient plasma parameters obtained from the IRI-95 ionospheric model[16] and MSIS-E-90 thermospheric model[17] provide

$$\rho_a^+(\boldsymbol{r}, t=0) + \rho_a^e(\boldsymbol{r}, t=0) + \rho_a(\boldsymbol{r}, t=0) \simeq 6.136 \times 10^{-12} \text{ kg/m}^3 \tag{45}$$

$$T_a^+(\boldsymbol{r}, t=0) = T_a^e(\boldsymbol{r}, t=0) = T_a(\boldsymbol{r}, t=0) = 1000 \text{ K} \tag{46}$$

It is also assumed that the ambient is initially stationary with

$$V_a^+(\boldsymbol{r}, t=0) = V_a(\boldsymbol{r}, t=0) = V_a^e(\boldsymbol{r}, t=0) = 0 \tag{47}$$

The ambient magnetic induction is based on PDP payload measurements and is given in the coordinate system indicated in Fig. 1 as

$$\boldsymbol{B}_a = (B_{xa} = 0,\ B_{ya} = 40{,}000,\ B_{za} = 22{,}000) \text{ nT} \tag{48}$$

The angle between the ETG-1 jet $\hat{\boldsymbol{x}}$ axis and the magnetic induction is close to 90 ± 10 deg, corresponding to an almost perpendicular direction. The angle between the PDP spin axis and the ambient induction is also close to 90 ± 10 deg.

Air-Cloud Initial Conditions

The air cloud was generated by a nozzle that operated for $\tau_0 = 0.2$ s prior to the ETG-1 detonation. The 1-cm^2 cross-section nozzle emitted $Q_c = 2.6 \times 10^{23}$ air particles in the $\hat{\boldsymbol{x}}$ direction as indicated in Fig. 1. Based on estimates[1] at the time of the ETG-1 detonation the air cloud had a density of up to $\rho_c = 10^{-6}$ kg/m^3

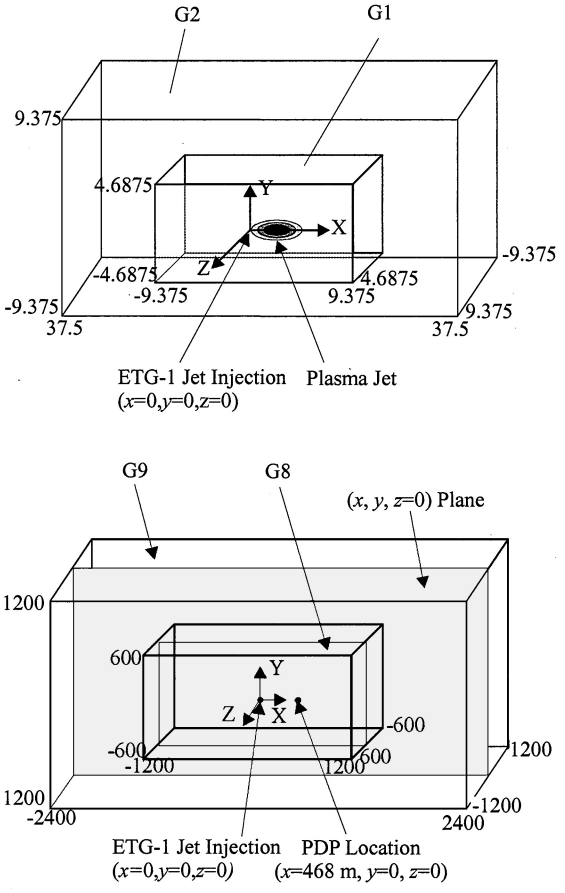

Fig. 3 Multigrids used in the simulation of the APEX ETG-1 plasma-jet experiment. The position of the PDP payload is depicted at $t = 0$ s, the time of the ETG-1 plasma-jet injection.

near the release point and had reached a distance of approximately 140 m away from ETG-1 with a density of $\rho_c = 10^{-9}$ kg/m^3. The initial conditions for the air cloud are derived with an implementation of a model developed for the expansion of a neutral plume.[18]

The expansion of the air cloud in the rarefied background for $t \ll \tau_0$ and distances close to the nozzle exit is in the continuum regime. As the air cloud expands, self-collisions become rare, and the flow is in a free-molecular regime. At later times collisions with the background become important, and the flow achieves a diffusion state.[5] A parameter that describes the behavior of a number Q_c of released air particles with molecular mass m_c released in the ambient is the equal mass radius given by

$$\alpha_0 = (3m_c Q_c / 4\pi n_a m_a)^{\frac{1}{3}} \tag{49}$$

The collision time between a released air-cloud molecule and the ambient neutrals is

$$\tau_{\text{ca}} = \nu_{\text{ca}}^{-1} = \left(\frac{8}{3\pi} n_a \frac{m_a}{m_c + m_a} \sqrt{\frac{2kT_{\text{ca}}}{\mu_{\text{ca}}}} \sigma_{\text{ca}} \right)^{-1} \text{s} \tag{50}$$

where $\mu_{\text{ca}} = m_c m_a/(m_c + m_a)$ is the reduced mass and $T_{\text{ca}} = (m_a T_c + m_c T_a)/(m_c + m_a)$ is the reduced temperature. The cross section is that of a hard-sphere molecule $\sigma_{\text{ca}} = \pi(r_c + r_a)^2$ where $r_c = 2.1 \times 10^{-10}$ m and $r_a = 2.0 \times 10^{-10}$ m are the radii of the air cloud and the ambient gas molecules, respectively. The corresponding mean free path for collisions is

$$\lambda_{\text{ca}} = \frac{3}{4} \frac{m_c + m_a}{m_a n_a \pi (r_c + r_a)^2} \text{ m} \tag{51}$$

Table 1 Computational parameters used in the multigrid simulations

Grid level	$L_x \times L_y \times L_z$, m	Δx, Δy, Δz, m	Δt, s	Grid simulation time, s	Total simulation time, s
G_1	$18.75 \times 9.375 \times 9.375$	0.25, 0.125, 0.125	5×10^{-10}	1.0×10^{-6}	1.0×10^{-6}
G_2	$3.57 \times 18.75 \times 18.75$	0.5, 0.25, 0.25	1×10^{-8}	2.0×10^{-5}	2.1×10^{-5}
G_3	$75 \times 37.5 \times 37.5$	1, 0.5, 0.5	5×10^{-8}	1.5×10^{-4}	1.7×10^{-4}
G_4	$150 \times 75 \times 75$	2, 1, 1	2×10^{-7}	4.5×10^{-4}	6.2×10^{-4}
G_5	$300 \times 150 \times 150$	4, 2, 2	4×10^{-7}	6.5×10^{-4}	1.3×10^{-3}
G_6	$600 \times 300 \times 300$	8, 4, 4	8×10^{-7}	6.5×10^{-4}	2.0×10^{-3}
G_7	$1200 \times 600 \times 600$	16, 8, 8	1×10^{-6}	4.0×10^{-3}	6.0×10^{-3}
G_8	$2400 \times 1200 \times 1200$	32, 16, 16	2×10^{-6}	7.0×10^{-3}	13×10^{-3}
G_9	$4800 \times 2400 \times 2400$	64, 32, 32	4×10^{-6}	14×10^{-3}	27×10^{-3}

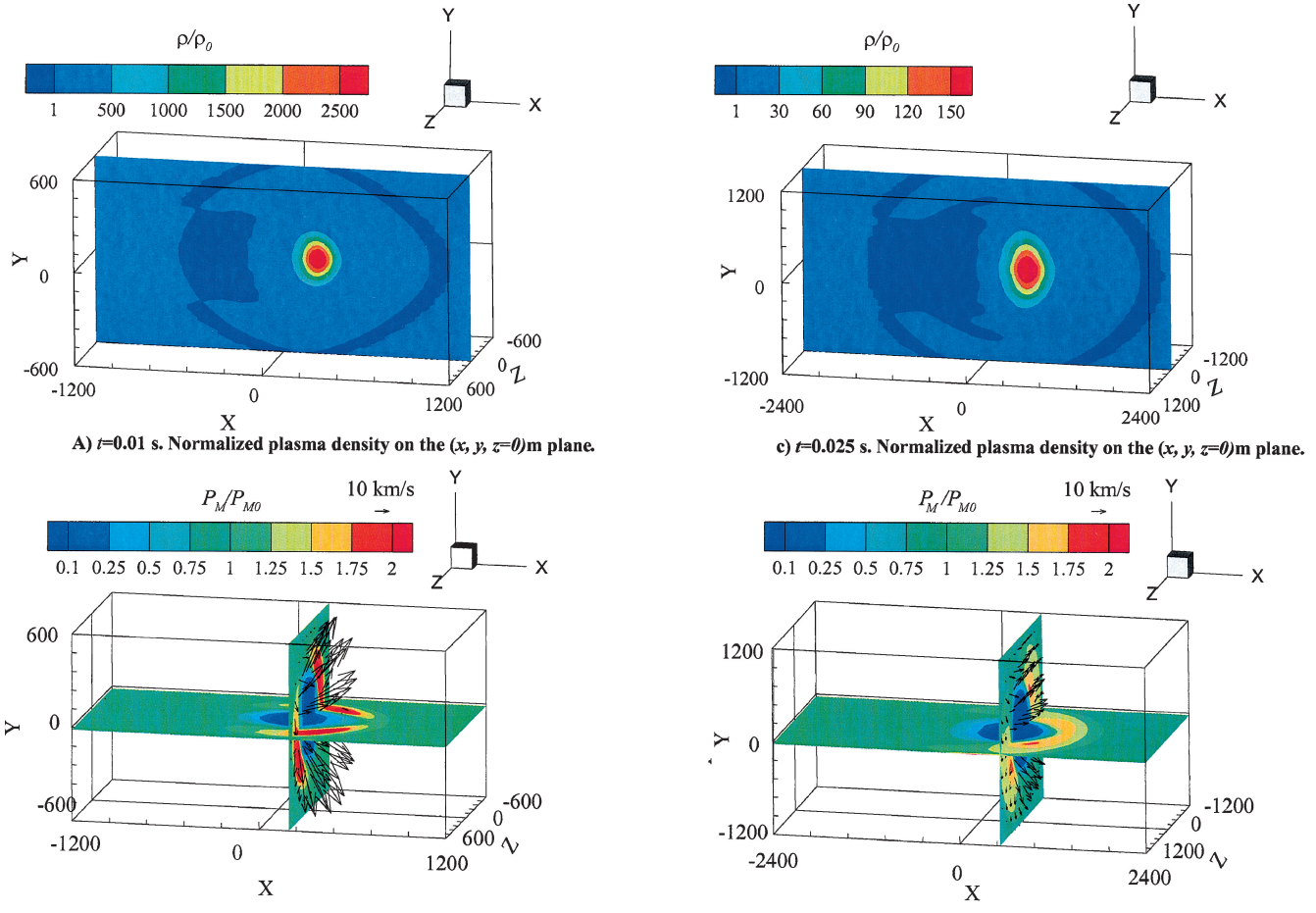

A) *t*=0.01 s. Normalized plasma density on the (*x, y, z=0*)m plane.

c) *t*=0.025 s. Normalized plasma density on the (*x, y, z=0*)m plane.

b) *t*= 0.01s. Normalized magnetic pressure on planes (*x, y=0, z*)m and (*x=227,y,z*)m with superimposed velocity vectors.

d) *t*= 0.025 s. Normalized magnetic pressure on planes (*x,y=0,z*)m and (*x=519,y,z*)m with superimposed velocity vectors

Fig. 4 Plasma properties from the simulation of the APEX ETG-1 plasma-jet experiment. The center of the plasma jet at $t = 0$ s was at ($x = 1.5$, $y = 0$, $z = 0$) m with velocity toward $\hat{x}$ perpendicular to $B_a = (B_{xa} = 0, B_{ya} = 40{,}000, B_{za} = 22{,}000)$ nT.

A ratio of $\alpha_o/\lambda \leq 3$ indicates free-molecular expansion for at least 1.4 mean collision times before interactions with the background become significant. For the conditions of the air-cloud release with $m_c = 4.7 \times 10^{-26}$ kg/particle and $Q_c = 2.6 \times 10^{23}$ particles, Eqs. (49–51) result in $\alpha_0 = 877$ m, $\tau_{ca} = 40$ s, and $\lambda_{ca} = 2.4 \times 10^4$ m. It is therefore expected that the air cloud will be in the free-molecular regime at the time of the ETG-1 detonation.

For times $t < \tau_0$ the macroscopic fluid properties of the air cloud are given by

$$\rho_c(r,\theta,t) = \frac{M_c}{4\pi\tau_0 r^2}\left(\frac{2m_c}{\pi k T_{sc}}\right)^{\frac{1}{2}} e^{-W_{sc}^2\sin^2\theta} \times \left[\pi^{\frac{1}{2}} W_{sc}\cos\theta\,\mathrm{erfc}(\alpha) + e^{-\alpha^2}\right] \tag{52}$$

$$\boldsymbol{V}_c(r,\theta,t) = \frac{\boldsymbol{r}}{r}\left(\frac{2kT_{sc}}{m_c}\right)\frac{(2W_{sc}\cos\theta+\alpha)e^{-a^2} - \sqrt{\pi}\left(W_{sc}^2\cos^2\theta + 0.5\right)\mathrm{erfc}(\alpha)}{e^{-a^2} + \sqrt{\pi}\,W_{sc}\cos\theta\,\mathrm{erfc}(\alpha)} \tag{53}$$

$$T_c(r,\theta,t) = \frac{2}{3}T_{sc} \tag{54}$$

In Eqs. (52–54) $r = \sqrt{(x^2+y^2+z^2)}$ is the radial position vector, θ is the angle between the air-cloud axis $\hat{\boldsymbol{x}}$, and the position vector

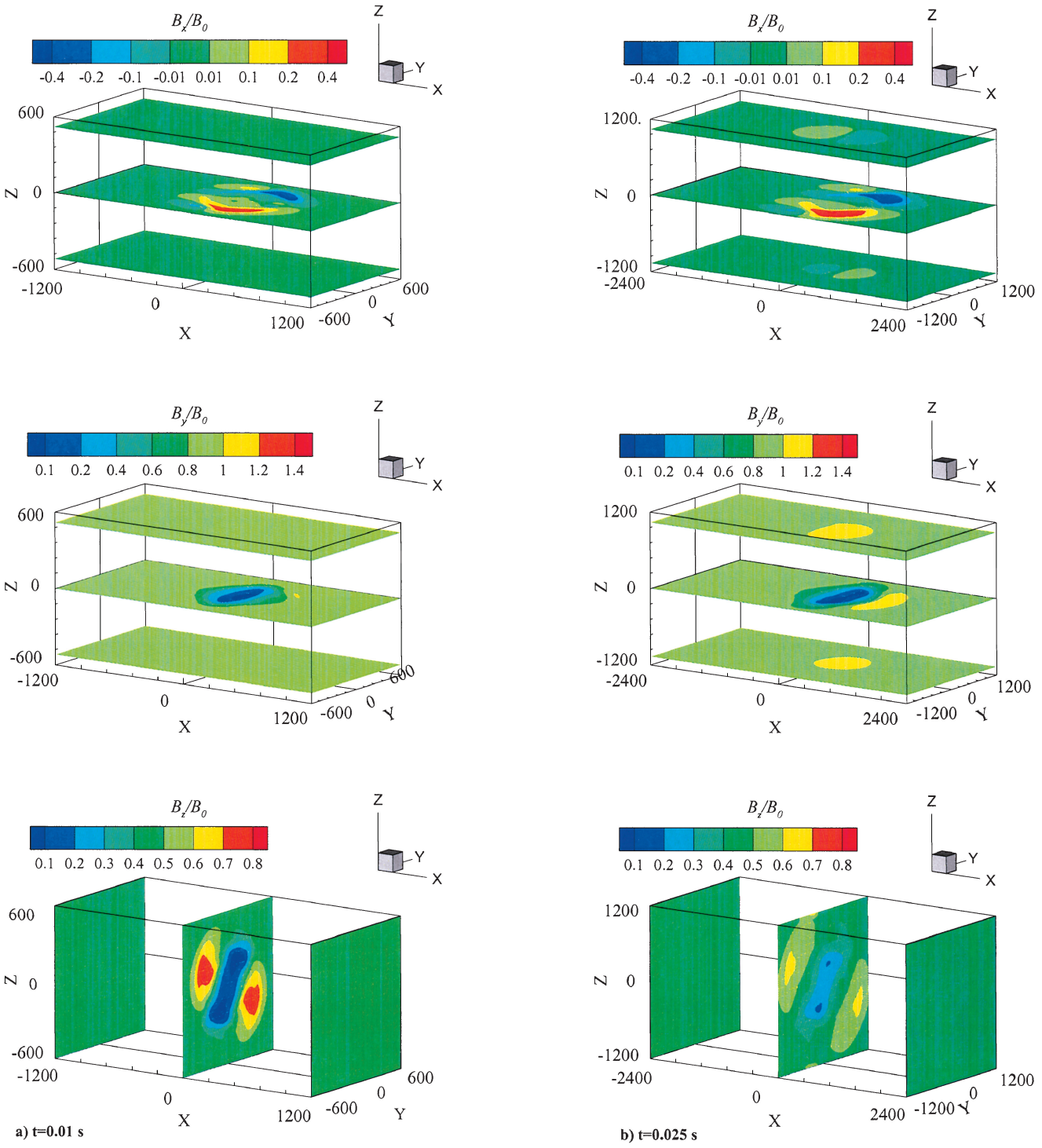

Fig. 5 Normalized magnetic induction components from the simulation of the APEX ETG-1 plasma-jet experiment at a) $t = 0.01$ s and b) $t = 0.025$ s. The center of the plasma jet at $t = 0$ s was at $(x = 1.5, y = 0, z = 0)$ m with velocity toward $\hat{x}$ perpendicular to $B_a = (B_{xa} = 0, B_{ya} = 40{,}000, B_{za} = 22{,}000)$ nT.

$\boldsymbol{r}$, and $\alpha = W_{sc}(r/u_{sc}\tau_0 - \cos\theta)$, where the molecular speed ratio is defined as

$$W_{sc} = u_{sc}\Big/\sqrt{2kT_{sc}/m_c} \tag{55}$$

The source conditions (u_{sc}, T_{sc}) are associated with the properties at the exit of the air-cloud nozzle (u_{ec}, T_{ec}) with velocity and temperature given by

$$u_{sc} = u_{ec}\left[\left(\gamma M_{ec}^2\right)^{-1} + 1\right] \tag{56}$$

$$T_{sc} = \frac{T_{ec}}{2}\frac{2\gamma M_{ec}^2 - \gamma + 1}{1 + \gamma M_{ec}^2} \tag{57}$$

$$W_{sc} = \frac{1 + \gamma M_{ec}^2}{\left(2\gamma M_{ec}^2 - \gamma + 1\right)^{\frac{1}{2}}} \tag{58}$$

The exit properties of the air-cloud nozzle are given by $u_{ec} = 700$ m/s, $T_{ec} = 60$ K, and $M_{ec} = 2$.

Plasma-Jet Initial Conditions

The ETG-1 plasma jet is assumed to be composed of singly ionized aluminum ions and electrons and the initial conditions are based on an analytical model that incorporates experimental parameters described next.

The ETG produces an aluminum high-speed plasma jet of total mass of about 30×10^{-3} kg, velocities in the range of 8000–40,000 m/s and a total kinetic energy of 6 MJ. Laboratory tests indicate that 92% of the jet energy is confined to within 20 deg from the jet axis, 10×10^{-3} kg exceed speeds of 10,000 m/s, 3×10^{-3} kg exceed 25,000 m/s, and 0.01×10^{-3} kg exceed 40,000 m/s. Based on these observations, the plasma jet is initialized with an axisymmetric density distribution given by

$$\rho_J(r, x, t=0) = \rho_j^+(r, x, t=0) + \rho_j^e(r, x, t=0)$$
$$= \rho_J^{\max}(1 - r/R_J)(1 - |2x - L_J|/L_J) \tag{59}$$

where $r = \sqrt{(y^2 + z^2)}$ shown in Fig. 1. The maximum plasma-jet density can be calculated from the total mass of the ETG-1 plasma given as

$$M_J = \int_0^{L_J}\int_0^{2\pi}\int_0^{R_J} \rho_J r\, \mathrm{d}r\, \mathrm{d}\phi\, \mathrm{d}x = \frac{\pi}{6}\rho_J^{\max} R_J^2 L_J \tag{60}$$

The ETG-1 plasma jet is approximated with an initial length of $L_J = 3$ m and radius $R_J = 0.75$ m. For $M_J = 30 \times 10^{-3}$ kg the resulting $\rho_J^{\max} = 34 \times 10^{-3}$ kg/m^3. Following experimental observations, the plasma-jet velocity is assumed to be directed along $\hat{\boldsymbol{x}}$ with a linear profile in the radial direction:

$$\boldsymbol{V}_j^+(r, t=0) = \boldsymbol{V}_j^e(r, t=0) = V_J^{\max}(1 - r/R_J)\hat{\boldsymbol{x}} \tag{61}$$

The maximum jet velocity $V_J^{\max}$ can be calculated from the total kinetic energy

$$E_J(t=0) = \int_0^{L_J}\int_0^{2\pi}\int_0^{R_J} \frac{\rho_J u_J^2}{2} r\, \mathrm{d}r\, \mathrm{d}\phi\, \mathrm{d}x = \frac{3}{20} M_J \left(V_J^{\max}\right)^2 \tag{62}$$

With $E_J = 6$ MJ, the resulting $V_J^{\max} = 37{,}000$ m/s. This jet model results in 80% of the aluminum mass to be within 20 deg of the jet's axis, 22×10^{-3} kg to have velocities in excess of 10,000 m/s, and 2×10^{-3} kg with velocities in excess of 25,000 m/s. The jet plasma is assumed to be isothermal with

$$T_j^+(r, t=0) = T_j^e(r, t=0) = 10{,}000 \text{ K} \tag{63}$$

Transport Coefficients and Boundary Conditions

The conductivity, viscosity, thermal conductivity given by Eqs. (13), (22), and (27) are evaluated using the initial plasma parameters and assumed to be constant during the simulation. Neumann boundary conditions $\partial \boldsymbol{W}/\partial \boldsymbol{n} = 0$ are applied to all boundary surface shown in Fig. 3, where $\boldsymbol{n}$ is the unit vector normal to a boundary and $\boldsymbol{W}$ is the state vector $\boldsymbol{W} = (\rho, u, v, w, p, B_x, B_y, B_z)^T$. This boundary condition is implemented using extrapolation from the interior grid nodes to the boundary nodes.

Multigrid Layering

The plasma jet in these simulations begins with meter-size length scales to reach 100-m scales at the time when it reaches the PDP instrument payload. The discretization requirements for such three-dimensional simulations are addressed by implementing a multigrid layering method outlined below.

The first $75 \times 75 \times 75$ orthogonal grid, denoted as G_1, is generated with dimensions of $L_x(G_1) = 18.75$ m, $L_y(G_1) = 9.375$ m, $L_z(G_1) = 9.375$ m with resulting grid sizes of $\Delta x(G_1) = 0.25$ m and $\Delta y(G_1) = \Delta z(G_1) = 0.125$ m. The G_1 simulation is stopped at 1.0×10^{-6} s before waves reach the boundary of the domain. The second $75 \times 75 \times 75$ grid designated by G_2 is generated with $L_x(G_2) = 2L_x(G_1)$, $L_y(G_2) = 2L_y(G_1)$, and $L_z(G_2) = 2L_z(G_1)$ and is shown schematically in Fig. 3. All G_1 flow variables are interpolated onto the G_2 grid and the simulation is continued. This procedure of generating a new grid doubling the size of the preceding one is repeated until the final grid covers the desired domain. A total of nine grid levels were used in the ETG-1 simulation, and the computational parameters are shown in Table 1. The total simulation time is 0.028 s, and we present results at times $t = 0.01$ s and 0.025 s obtained on G_8 and G_9 grids respectively shown in Fig. 3.

Discussion of Results

In Fig. 4, the nondimensional density is plotted on the $(x, y, z = 0)$ plane. At initialization of the simulation, the jet center was located at $(x = 1.5, y = 0, z = 0)$ m with a maximum of $\rho/\rho_0 = 10^{10}$, where $\rho_0 = 10^{-12}$ kg/m^3. A comparison between Figs. 4a and 4c shows that the plasma jet has moved downstream from the injection point and formed a density structure elongated along $\hat{\boldsymbol{x}}$ and $\hat{\boldsymbol{y}}$. At $t = 0.01$ s the maximum density is $\rho/\rho_0 \simeq 3313$ and is located at $(x = 227, y = 0, z = 0)$ m downstream of the injection point corresponding to an average speed of 22,800 m/s. At $t = 0.025$ s the density maximum reduces to $\rho/\rho_0 \simeq 205$ and is

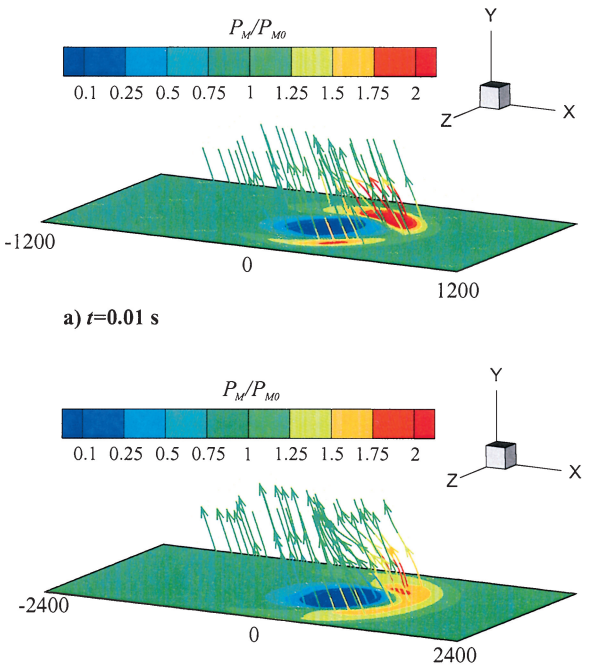

Fig. 6 Isolines of the magnetic induction B superimposed on the normalized magnetic pressure on the plane $(x, z, y = 0)$ m from the simulation of the APEX ETG-1 plasma-jet experiment. The center of the plasma jet was initially at $(x = 1.5, y = 0, z = 0)$ m with velocity toward $\hat{x}$, perpendicular to $B_a = (B_{xa} = 0, B_{ya} = 40{,}000, B_{za} = 22{,}000)$ nT.

located at ($x = 519$, $y = 0$, $z = 0$) m corresponding to an average speed of 20,860 m/s.

In Figs. 4b and 4d the velocity vectors are plotted on the ($x = 227$, $y = 0$, $z = 0$) m and ($x = 519$, $y = 0$, $z = 0$) m planes, respectively. As Eq. (61) shows, the plasma jet was initialized with velocity in the $\hat{\boldsymbol{x}}$ direction and a maximum of 38,000 m/s. However, Figs. 4b and 4d show the development of velocity components in the $\hat{\boldsymbol{y}}$ and $\hat{\boldsymbol{z}}$ directions as the plasma expands along the ambient magnetic field. The jet decelerates considerably as a result of the interaction with the background plasma. Figure 4 shows also that the plasma at spatial locations outside the jet region is set into motion. The induced motion in the background plasma is the result of the expansion process as well as the momentum coupling through waves that are propagating into the background.

To gain further insight into the physical mechanism of the plasma-jet motion, we investigate the magnetic pressure. In Figs. 4c and 4d the normalized magnetic pressure P_M/P_{M0}, where $P_{M0} = 8.29 \times 10^{-4}$ Pa, is plotted on planes passing through the density maxima located at ($x = 227$, $y = 0$, $z = 0$) m at $t = 0.01$ s and ($x = 519$, $y = 0$, $z = 0$) m $t = 0.025$ s. The simulation predicts the formation of a cavity with a local minimum at its core of $P_M/P_{M0} = 6.84 \times 10^{-3}$ and 9.8×10^{-3} at $t = 0.01$ and 0.025 s, respectively. This indicates a gradual weakening of the cavity as a result of the corresponding decrease it the jet density. The local maxima on the $x - z$ plane are ahead of the plasma jet with $P_M/P_{M0} = 2.372$ and $P_M/P_{M0} = 2.266$ at $t = 0.01$ and 0.025 s, respectively. The local maxima on the planes through the center of the plasma jet are $P_M/P_{M0} = 2.269$ and 1.799 at $t = 0.01$ and 0.025 s, respectively. The asymmetry of the magnetic pressure barrier on the $y - z$ plane is caused by the presence of both $B_{\rm za}$ and $B_{\rm ya}$ components of the ambient induction.

The components of magnetic induction normalized with $B_0 = B_a = 4.56 \times 10^{-5}$ T are plotted in Fig. 5 for times of $t = 0.01$ and 0.025 s after the ETG-1 injection. Perturbations in the form of enhancements or depletions over the uniform ambient induction at $t = 0$s appear in all three components. This complex MHD wave structure emanates from the jet region and propagates in the ambient plasma region toward the boundaries as a comparison between Figs. 5a and 5b shows. Figure 5 shows the development of a perturbation in B_x in the form of a depletion and an enhancement region, which is elongated in the direction of the jet motion. At $t = 0.025$ s the perturbations in B_x reach the upper and lower boundaries of the domain. The B_y component shows the formation of a cavity that coincides with the jet and an enhancement region ahead of the jet. This enhancement is related to a magnetosonic wave that propagates perpendicular to $\boldsymbol{B}_a$. The B_z component forms a depletion and enhancement structure that is elongated along the direction of $\boldsymbol{B}_a$ and diminishes in magnitude with time as a comparison between Figs. 5a and 5b shows.

The picture that emerges from the simulation is consistent with a slowing-down process of the three-dimensional plasma jet as a result of loss of jet kinetic energy by joule dissipation and viscous effects. The ambient field opposes the motion perpendicular to the field lines but leaves practically uninhibited the motion along the field lines. In Fig. 6 the magnetic field isolines illustrate the process of generation of Alfvén waves. The induced and ambient field result in a magnetic field that is inclined with the direction if the jet. This gives rise to a Lorentz force that opposes the jet motion and causes disturbances to propagate along and transverse to the field lines. The MHD wave structure resulting from the ETG-1 plasma jet is fully three dimensional and dissipative in nature.

Comparisons with Data and Interpretation of Results

To compare the simulation results with data taken onboard the PDP payload, a virtual probe was inserted in the simulation at a distance of $x = 468$ m downstream of the injection point, in a configuration shown schematically in Fig. 3. This placement of the virtual probe ignores the approximately 54-m displacement of the PDP from its initial position during the simulation time 27×10^{-3} s. The placement also assumes a perpendicular orientation of the PDP and its sensors with the jet axis and the ambient magnetic field.

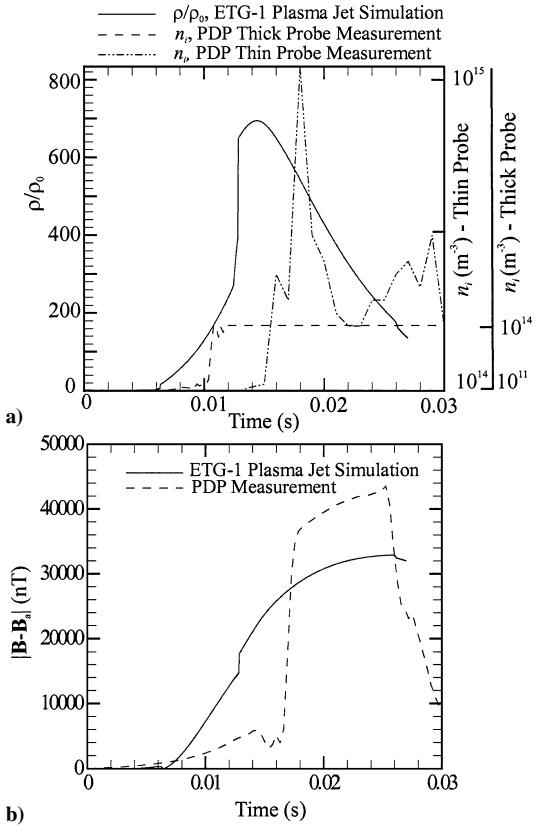

Fig. 7 Predictions of plasma density and magnetic induction perturbation from the simulation of the APEX ETG-1 plasma-jet experiment. Measurements are from the Langmuir probes and the fluxgate magnetometer onboard the PDP payload. The virtual payload in the simulation is placed at 468 m downstream of the plasma-jet injection location to coincide with the approximate position of the PDP payload.

The relative displacement and orientation characteristics of the PDP are ignored in our simulations because they relate to spatial scales smaller than the grid sizes used in the G_9 simulation (Table 1).

Figure 7a shows the nondimensional plasma density ρ/ρ_0 as a function of time and compares it with the plasma number density derived from the two cylindrical Langmuir probes onboard the PDP.[19] The thick probe had a radius of 5×10^{-3} m, length of 100×10^{-3} m, sampling rate 100 kHz, and range 10^{10}–10^{14} m^{-3}. The thin probe had a radius of 0.5×10^{-3} m, length of 50×10^{-3} m, sampling rate 50 kHz, and range of 10^{14}–10^{19} m^{-3}. The simulation predicts the arrival of the density somewhat earlier than the thin probe; however, it shows the rapid increase and slower decrease as the back of the plasma jest passes by the virtual sensor.

An important parameter in the evaluation of the plasma-jet/ambient interactions is the strength of the diamagnetic cavity predicted by the simulation and recorded also onboard the PDP. The magnetic induction perturbation is defined by

$$|\boldsymbol{B} - \boldsymbol{B}_a| = \sqrt{\Delta B_x^2 + \Delta B_y^2 + \Delta B_z^2} \tag{64}$$

where

$$\Delta B_i = B_i - B_{\rm ia}, \qquad i = x, y, z \tag{65}$$

In Fig. 7b the diamagnetic cavity is shown to reach the virtual probe at $t \simeq 0.006$ s and increase gradually in magnitude to reach a maximum of 30,000 nT at $t = 0.026$ s. The PDP magnetometer recorded a faster increase that reached 44,000 nT at $t = 0.026$ indicating an almost complete reduction of the ambient magnetic induction with $B_a = 46{,}000$ nT (Ref. 15). The differences indicate that the simulation predicted a spatially larger cavity formation with reduced strength.

The components of the magnetic-induction perturbation are plotted in Fig. 8. Along the direction of the jet motion, the PDP recorded

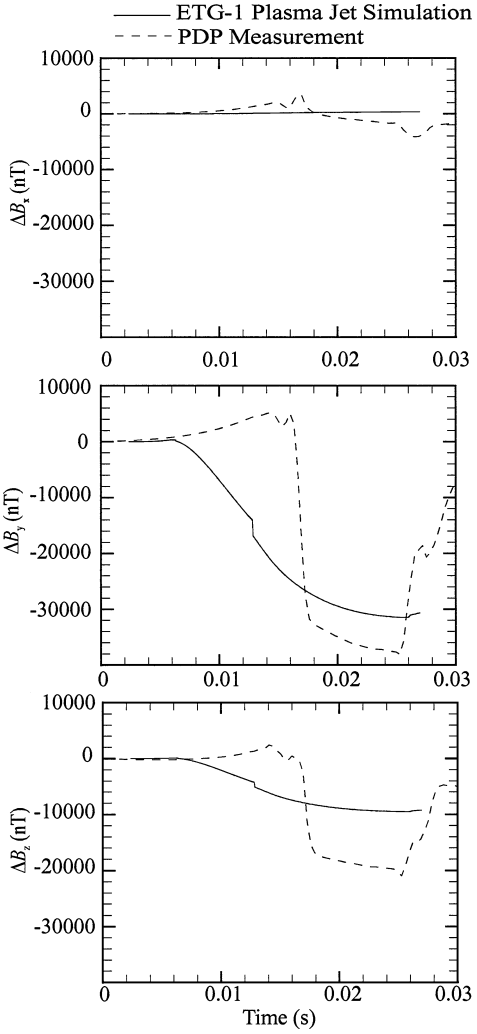

Fig. 8 Predictions of magnetic induction perturbation components from the simulation of the APEX ETG-1 plasma-jet experiment. Measurements are from the fluxgate magnetometer onboard the PDP payload. The virtual probe in the simulation is placed 468 m downstream of the plasma-jet injection location to coincide with the approximate position of the PDP payload. The plasma-jet velocity is initially in the $\hat{x}$ direction, perpendicular to $\boldsymbol{B}_a = (B_{xa} = 0, B_{ya} = 40{,}000, B_{za} = 22{,}000)$ nT.

an increase in the magnetic induction of about 4000 followed by a reduction of about 4000 nT. The simulation predicted an increase of less than 100 nT. The y component shows an increase of about 4000 nT over the ambient followed by a sharp reduction leading to a minimum of $-38{,}000$ nT. The simulation predicts a monotonic decrease from the ambient B_{za} that reaches a minimum of $-30{,}000$ nT at $t = 0.026$ s. The z component of the magnetic induction decreases to reach a value of 20,000 nT below its ambient level while the simulation predicts a reduction of about 10,000 nT occurring at $t = 0.026$ s.

The preceding predictions are capturing the essential features of the diamagnetic cavity formation and follow quantitatively and qualitatively the data recorded onboard the PDP payload. Differences between the simulation and measurements can be attributed to sources that include modeling limitations as well as experimental uncertainties discussed next.

One of the goals of the APEX experiment was to explore the role of the neutral air cloud on the plasma-jet dynamics. The presence of the air cloud during the ETG-1 jet injection contributed to the increased ionization observed over the ETG-2 injection that was not preceded by an air cloud. In addition, the ETG-1 plasma jet was somewhat slower as compared to the ETG-2 plasma jet.[1,19] These observations are consistent with the presence of the air cloud during the ETG-1 injection although the difference in the jet orientation between the two experiments might have contributed as well. In the present MHD work the effects of the air cloud are incorporated into the simulation because the air cloud is one of the species that forms at initialization the single-fluid plasma properties as shown in Eqs. (42–44). However, after initialization the MHD model cannot provide the properties of the components that form the single-fluid plasma. Therefore, the single-fluid (MHD) model limits the insights on the interactions between the ionized and neutral components of the jet-ambient plasma system. The role of a neutral velocity field (or wind) applied on to a plasma has been explored extensively in ionospheric dynamics[20] and plasma cloud dynamics.[5–7] Within a steady-state, multifluid formulation of a plasma, it has been shown that a neutral velocity component transverses to the $\boldsymbol{B}$ field when applied to a plasma, induces an ion velocity that is at an angle with the applied neutral velocity, and depends on $\beta_i = \Omega_i/\nu_i$ (Refs. 6, 7, and 20). In contrast, a neutral velocity component parallel to the $\boldsymbol{B}$-field induces a plasma drift along its direction. The presence of a neutral cloud leads also to collisional drag that can resist the motion of a plasma. The single-fluid character of our model does not allow also for the investigation of ionization phenomena, including the possibility of critical ionization velocity, as the plasma jet passes through the neutral cloud.[1] Such competing effects and their role on plasma jet dynamics can be investigated only with a multifluid formulation.

Another goal of the APEX experiment was the investigation of jet/ambient current closure patterns. In an MHD approximation similar to one followed in the present work, the current closure is described effectively with Ohm's law utilized. In the present study Ohm's law equation (12) does not include the Hall and ion slip currents because of the assumption of a collision-dominated plasma, and we explore below the implications. With an estimated value of $B = 450$ nT in the diamagnetic cavity and $B = 45{,}000$ nT in the ambient plasma, the resulting gyrofrequencies for electrons is $\Omega_e = 7.9 \times 10^4$ and 7.9×10^6 Hz, respectively. The evaluation of electron collision frequencies for the partially ionized ETG-1 plasma environment must include electron-ion and electron-neutral collisions given by[9]

$$\nu_{\mathrm{ei}} = 3.64 \times 10^{-6}\left(Z_i^2 \big/ T_e^{\frac{3}{2}}\right) n_i \, \ell_n \Lambda_{\mathrm{ei}} \tag{66}$$

$$\nu_{\mathrm{en}} \simeq n_n Q_{\mathrm{en}} \sqrt{8kT_e/\pi m_e} \tag{67}$$

With an ion number density of approximately 3×10^{15} m^{-3} and assuming $T_e = 11{,}604$ K at the PDP and the ETG-2 payload,[19] Eq. (66) results in $\nu_{\mathrm{ei}} \approx 8.7 \times 10^4$ s^{-1}. The neutral air-cloud number density is estimated at 2×10^{16} m^{-3} at 140 m from the release point and with $Q_{\mathrm{en}} \simeq 10^{-19}$ m^{-2}, Eq. (67) results in $\nu_{\mathrm{en}} \simeq 1.4 \times 10^3$ s^{-1}. Near the release point the neutral density can be up to $n_c \approx 2 \times 10^{19}$ m^{-3}, and the collision frequency can be $\nu_{\mathrm{en}} \approx 1.4 \times 10^6$ s^{-1}. In the background plasma the electron collision frequencies are $\nu_{\mathrm{ei}} \approx 146$ s^{-1} and 4.8 s^{-1}. Therefore, $\beta_e = \Omega_e/(\nu_{\mathrm{ei}} + \nu_{\mathrm{en}})$ can be as small as 0.053 inside the dense parts of the jet, but the electrons will be collisionless with $\beta_e \gg 1$ in the ambient plasma. The aluminum ions have $\Omega_i = 1.6$ Hz in the diamagnetic cavity and $\Omega_i = 160$ Hz in the ambient plasma. Therefore, the ions are collision dominated $\beta_i \ll 1$ or $\beta_i \leq \mathcal{O}(1)$ in the jet region but are collisionless in the ambient, that is, $\beta_i > 1$. The condition $S \ll 1$ is satisfied for the plasma jet but becomes questionable in the ambient. In a single-fluid (MHD) framework the so-called generalized Ohm's law with Hall and ion-slip terms included would be identical to the tensor conductivity with the B field in the z direction as expressed by

$$\begin{bmatrix} J_x \\ J_y \\ J_z \end{bmatrix} = \begin{bmatrix} \sigma_P & \sigma_H & 0 \\ \sigma_H & \sigma_P & 0 \\ 0 & 0 & \sigma_0 \end{bmatrix} \begin{bmatrix} E'_x \\ E'_y \\ E'_z \end{bmatrix} \tag{68}$$

The current system in the jet-ambient plasma involves Pedersen, Hall, and parallel conductivities that include contribution form the ions and electrons.[9] The omission of the Hall term in Ohm's law

equation (12) leads to the absence of Hall currents and also to an isotropic conductivity expressed by Eq. (13). However, in the transverse to the $\boldsymbol{B}$-field direction the currents in the jet and the ambient ionospheric plasma at the altitude of the ETG-1 experiment are mainly caused by the ionic Pedersen conductivity despite the fact that the electron currents flow mainly as a result of the Hall conductivity. Therefore, the omission of Hall currents in our model is not expected to affect the results in a significant way. The omission of ion slip in Ohm's law implies that the electron current density parallel to the B field is much larger than the ion current density.

In general, the current closure between the jet ambient is more complex than what the simplified Ohm's law used in this study or a generalized Ohm's law with Hall and ion slip terms can describe. The current density includes a direct current due to electric field expressed with a conductivity tensor similar to Eq. (68), a diamagnetic current due to density gradients, a current due a neutral field (winds) and a current due to gravity.[5,6] The Alfvén waves contribute additional currents and can change the picture of plasma-jet dynamics. In previous work[5–7] a layer model for the plasma jet showed that inclusion of Alfvén waves leads to smaller perturbation fields within the plasma jet, a result of larger parallel currents that depolarize charge accumulation within the plasma jet. The Alfvén waves are included self-consistently on our MGD formulation despite the fact that they do not explicitly appear in Ohm's law. The current closure with the Alfvén waves is explored in the hybrid APEX-jet simulation of Delamere et al.[21]

The initial conditions for the air cloud and the aluminum plasma jet were developed from limited laboratory data and as such might have contributed to the differences between observations and predictions. The ETG-1 jet plasma model in particular is represented by an axisymmetric density distribution equation (59) and a unidirectional velocity distribution equation (61). Our simulations show that the maximum jet velocity is reduced at the location of the PDP, but the arrival time of the jet and the steepening characteristics of the jet front are sensitive to the physical parameters at the time of the ETG-1 injection. A more advanced treatment would require simulations of the aluminum jet inside the ETG nozzle that would then be used as initial data for a large-scale single-fluid simulation. The spatial discretization is expected to induce also some numerical diffusion and reduce the magnitude of sharp gradients that appear naturally. A grid-adaptation strategy might have been more successful in eliminating numerical diffusion.

The direction of the jet axis and the PDP spin axis with respect to the ambient magnetic field are known within a ± 10-deg accuracy. Therefore, the PDP and its sensors could very well be off the ETG-1 jet centerline while our virtual probe is placed directly at the centerline of the jet. The ETG-1 simulation as well as the simulations of the Fluxus aluminum jet experiments[12,22] show that the jet expansion is a fully three-dimensional process; therefore, the magnitude and evolution of magnetic and density perturbations depend on the position of the virtual probe. The three dimensionality of the expansion process is further verified by the results of the ETG-2 injection.[1] The PDP spin axis during the ETG-2 injection was at large angles with the jet axis (up to 80 deg), and the jet axis recorded the presence of the jet but did not record the formation of a diamagnetic cavity. The uncertainty of the PDP attitude with respect to the jet axis introduces also a complexity in the interpretation of the magnetic field components as measured on the local PDP coordinates. Our simulations could not predict the initial enhancement of the components of the magnetic field before the formation of the diamagnetic cavity as shown in Fig. 8. This enhancement coincides temporally with the density increase detected by the thick probe and can be related to the early arrival of waves. The early density saturation on the thick probe can be related to electron photoemission before the arrival of the jet itself. Finally, it should be pointed that current collection by cylindrical Langmuir probes in flowing plasmas is highly dependent on the incident angle[23] while the number densities inferred by the cylindrical PDP probes assumed a parallel orientation.[19] Clearly, because of the discretization limitations in the large-scale simulations performed here, the geometrical features of PDP sensors and orientation could not be included.

Conclusions

This work presented the modeling and simulation of the aluminum plasma jet injected in the ionosphere by the explosive-type generator (ETG)–1 during the APEX North Star Mission. The simulation is based on a three-dimensional model of the aluminum plasma jet, the air cloud, and the ambient ionospheric plasma, using the single-fluid, unsteady, compressible, viscous, magnetohydrodynamic (MHD) equations. The simulations revealed complex interactions between the plasma jet and the ambient magnetized plasma. Some of the important features captured by the simulation include the formation of a diamagnetic cavity, the formation of a complex pattern of magntetohydrodynamic waves, the deceleration of the jet, and the induced motion in the background plasma. Comparisons with the density and magnetic induction data taken onboard the PDP payload located at about 468 m from the injection point show good overall qualitative and quantitative agreement. The simulation predicts the formation of a diamagnetic cavity with a 30,000-nT depletion of the ambient value. The magnetic induction components show the presence of a small perturbation in the direction perpendicular to the ambient induction and large perturbations on the plane of the ambient induction. The simulations show that large-scale jet-ambient plasma interactions can be modeled effectively with single-fluid formulations based on the viscous MHD equations.

Appendix: Nondimensional Flux Vectors

$$\boldsymbol{g}_I^* = \left[\rho^* v^*, \rho^* u^* v^*, \rho^* v^{*2} + p^*, \rho^* v^* w^*, v^* \frac{\gamma p^*}{(\gamma - 1)} + \frac{\rho^* v^* (u^{*2} + v^{*2} + w^{*2})}{2}, 0, 0, 0\right]^T \tag{A1}$$

$$\boldsymbol{h}_I^* = \left[\rho^* w^*, \rho^* w^* u^*, \rho^* u^* v^*, \rho^* w^{*2} + p^*, w^* \frac{\gamma p^*}{(\gamma - 1)} + \frac{\rho^* w^* (u^{*2} + v^{*2} + w^{*2})}{2}, 0, 0, 0\right]^T \tag{A2}$$

$$\boldsymbol{g}_V^* = \left[0, -\frac{\mu_v^*}{Re_0}\left(\frac{\partial u^*}{\partial y^*} + \frac{\partial v^*}{\partial x^*}\right), -\frac{2\mu_v^*}{3Re_0}\left(2\frac{\partial v^*}{\partial y^*} - \frac{\partial u^*}{\partial x^*} - \frac{\partial w^*}{\partial z^*}\right), -\frac{\mu_v^*}{Re_0}\left(\frac{\partial v^*}{\partial z^*} + \frac{\partial w^*}{\partial y^*}\right), -\frac{\mu_v^*}{Re_0}\left(\frac{\partial u^*}{\partial y^*} + \frac{\partial v^*}{\partial x^*}\right) u^* - \frac{2\mu_v^*}{3Re_0}\left(2\frac{\partial v^*}{\partial y^*} - \frac{\partial u^*}{\partial x^*} - \frac{\partial w^*}{\partial z^*}\right) v^* - \frac{\mu_v^*}{Re_0}\left(\frac{\partial v^*}{\partial z^*} + \frac{\partial w^*}{\partial y^*}\right) w^* + \frac{\mu_v^*}{(\gamma - 1) M_0^2 Re_0 Pr}\frac{\partial T^*}{\partial y^*}, 0, 0, 0\right]^T \tag{A3}$$

$$\boldsymbol{h}_V^* = \left[0, -\frac{\mu_v^*}{Re_0}\left(\frac{\partial u^*}{\partial z^*} + \frac{\partial w^*}{\partial x^*}\right), -\frac{\mu_v^*}{Re_0}\left(\frac{\partial v^*}{\partial z^*} + \frac{\partial w^*}{\partial y^*}\right), -\frac{2\mu_v^*}{3Re_0}\left(2\frac{\partial w^*}{\partial z^*} - \frac{\partial u^*}{\partial x^*} - \frac{\partial v^*}{\partial y^*}\right), -\frac{\mu_v^*}{Re_0}\left(\frac{\partial u^*}{\partial z^*} + \frac{\partial w^*}{\partial x^*}\right) u^* - \frac{\mu_v^*}{Re_0}\left(\frac{\partial v^*}{\partial z^*} + \frac{\partial w^*}{\partial y^*}\right) v^* - \frac{2\mu_v^*}{3Re_0}\left(2\frac{\partial w^*}{\partial z^*} - \frac{\partial u^*}{\partial x^*} - \frac{\partial v^*}{\partial y^*}\right) w^* + \frac{\mu_v^*}{(\gamma - 1) M_0^2 Re_0 Pr}\frac{\partial T^*}{\partial z^*}, 0, 0, 0\right]^T \tag{A4}$$

$$\boldsymbol{g}^*_{M1} = \Bigg[0, -\frac{1}{\mu^* M^2_{M0}} B^*_y B^*_x, -\frac{1}{2\mu^* M^2_{M0}}\left(B^{*2}_y - B^{*2}_x - B^{*2}_z\right), -\frac{1}{\mu^* M^2_{M0}} B^*_y B^*_z, \frac{\left[v^*\left(B^{*2}_x + B^{*2}_y + B^{*2}_z\right) - B^*_y\left(u^* B^*_x + v^* B^*_y + w^* B^*_z\right)\right]}{2\mu^* M^2_{M0}}, -u^* B^*_y + v^* B^*_y, 0, -v^* B^*_z + w^* B^*_y\Bigg]^T \tag{A5}$$

$$\boldsymbol{h}^*_{M1} = \Bigg[0, -\frac{1}{\mu^* M^2_{M0}} B^*_z B^*_x, -\frac{1}{\mu^* M^2_{M0}} B^*_z B^*_y, -\frac{1}{2\mu^* M^2_{M0}}\left(B^{*2}_z - B^{*2}_x - B^{*2}_y\right), \frac{\left[w^*\left(B^{*2}_x + B^{*2}_y + B^{*2}_z\right) - B^*_z\left(u^* B^*_x + v^* B^*_y + w^* B^*_z\right)\right]}{2\mu^* M^2_{M0}}, -u^* B^*_z + w^* B^*_x, -v^* B^*_z + w^* B^*_y, 0\Bigg]^T \tag{A6}$$

$$\boldsymbol{g}^*_{M2} = \Bigg[0, 0, 0, 0, \frac{1}{Re_{M0} M^2_{M0} \mu^{*2} \sigma^*}\Bigg[B^*_z\left(\frac{\partial B^*_y}{\partial z^*} - \frac{\partial B^*_z}{\partial y^*}\right) + B^*_x\left(\frac{\partial B^*_y}{\partial x^*} - \frac{\partial B^*_x}{\partial y^*}\right)\Bigg], -\frac{1}{Re_{M0}\mu^*\sigma^*}\left(\frac{\partial B^*_y}{\partial x^*} - \frac{\partial B^*_x}{\partial y^*}\right), 0, \frac{1}{Re_{M0}\mu^*\sigma^*}\left(\frac{\partial B^*_z}{\partial y^*} - \frac{\partial B^*_y}{\partial z^*}\right)\Bigg] \tag{A7}$$

$$\boldsymbol{h}^*_{M2} = \Bigg[0, 0, 0, 0, \frac{1}{Re_{M0} M^2_{M0} \mu^{*2} \sigma^*}\Bigg[B^*_x\left(\frac{\partial B^*_z}{\partial x^*} - \frac{\partial B^*_x}{\partial z^*}\right) + B^*_y\left(\frac{\partial B^*_z}{\partial y^*} - \frac{\partial B^*_y}{\partial z^*}\right)\Bigg], \frac{1}{Re_{M0}\mu^*\sigma^*}\left(\frac{\partial B^*_x}{\partial z^*} - \frac{\partial B^*_z}{\partial x^*}\right), -\frac{1}{Re_{M0}\mu^*\sigma^*}\left(\frac{\partial B^*_z}{\partial y^*} - \frac{\partial B^*_y}{\partial z^*}\right), 0\Bigg] \tag{A8}$$

References

[1]Erlandson, R. E., Meng, C. I., Swaminathan, P. K., Kumar, C. K., Dogra, V. K., Stoyanov, B. J., Gavrilov, B. G., Kiselev, Y., Zetzer, J. I., Stenbaek-Nielsen, H. C., Lynch, K. A., Pfaff, R. F., Delamere, P. A., Bounds, S., and Gatsonis, N. A., "North Star Plasma-Jet Space Experiment," *Journal of Spacecraft and Rockets*, Vol. 41, No. 4, 2004, pp. 483–489.

[2]Boyd, I. D., and Ketsdever, A. (eds.), "Special Section: Interactions Between Spacecraft and Thruster Plumes," *Journal of Spacecraft and Rockets*, Vol. 38, No. 3, 2001, pp. 380–464.

[3]Raizer, Y. P., and Surzhikov, S. T., "High-Altitude Explosions and Their Magnetohydrodynamic Description," *AIAA Journal*, Vol. 33, No. 2, 1995, pp. 479–490.

[4]Raizer, Yu. P., and Surzhikov, S. T., "Magnetohydrodynamic Description of Collisionless Plasma Expansion in Upper Atmosphere," *AIAA Journal*, Vol. 33, No. 2, 1995, pp. 486–490.

[5]Gatsonis, N. A., Tsuda, K., and Erlandson, R. E., "3-D Multi-Fluid Modeling of Aluminum Plasma Jets in the Ionosphere," AIAA Paper 98-2428, June 1998.

[6]Gatsonis, N. A., and Hastings, D. E., "A Three-Dimensional Model and Initial Time Numerical Simulation of an Artificial Plasma Cloud in the Ionosphere," *Journal of Geophysical Research—Space Physics*, Vol. 96, No. A5, 1991, pp. 8623–8639.

[7]Gatsonis, N. A., and Hastings, D. E., "Evolution of the Plasma Environment Induced Around Spacecraft by Gas Releases: Three-Dimensional Modeling," *Journal of Geophysical Research—Space Physics*, Vol. 98, No. A10, 1992, pp. 14,980–15,005.

[8]Gatsonis, N. A., Andreeva, T., and Erlandson, R. E., "Magnetogasdynamic Modeling of Plasma Expansion in Magnetic Field," AIAA Paper 99-3835, July 1999.

[9]Mitchner, M., and Kruger, C. H., *Partially Ionized Gases*, Wiley, New York, 1992.

[10]Jameson, A., Schmidt, W., and Turkel, E., "Numerical Solutions of the Euler Equations by Finite Volume Method Using Runge–Kutta Time-Stepping Schemes," AIAA Paper 81-1259, June 1981.

[11]Swanson, R. C., and Turkel, E., "A Multistage Time-Stepping Scheme for the Navier–Stokes Equations," AIAA Paper 85-0035, Jan. 1985.

[12]Andreeva, T., "Magnetogasdynamic Modeling of the FLUXUS Plasma Jets Injected in the Ionosphere," M.S. Thesis, Worcester Polytechnic Inst., Worcester, MA, Sept. 1999.

[13]Demagistris, M., "Magnetogasdynamic Modeling of the APEX North Star Plasma Jet Space Experiment," M.S. Thesis, Worcester Polytechnic Inst., Worcester, MA, April, 2001.

[14]Brackbill, J. U., and Barnes, D. C., "The Effects of Nonzero $\nabla \cdot \boldsymbol{B}$ on the Numerical Solution of the Magnetohydrodynamic Equations," *Journal of of Computational Physics*, Vol. 35, No. 11, 1980, p. 426.

[15]Pfaff, R. F., Freudenreich, H. T., Bounds, S., Delamere, P. A., Erlandson, R. E., Meng, C. I., Zetzer, J. I., and Gavrilov, B. G., "Electric Field, Magnetic Field, and Density Measurements on the Active Plasma Experiment," *Journal of Spacecraft and Rockets*, Vol. 41, No. 4, 2004, pp. 521–532.

[16]National Space Science Data Center, International Reference Ionosphere, IRI-95 Model, Ver. 1.0, NASA Goddard Space Flight Center, Greenbelt, MD, Oct. 1996.

[17]National Space Science Data Center, MSIS-E-90 Atmospheric Model, Ver. 1.0, NASA Goddard Space Flight Center, Greenbelt, MD, Oct. 1995.

[18]Baum, H. R., "The Interaction of a Transient Exhaust Plume with a Rarefied Atmosphere," *Journal of Fluid Mechanics*, Vol. 58, 1973, pp. 895–815.

[19]Gavrilov, B. G., Podgorny, I. M., Sobyanin, D. B., Zetzer, J. I., Erlandson, R. E., Meng, C. I., Pfaff, R. F., and Lynch, K. A., "North Star Plasma-Jet Experiment Particles and Electric and Magnetic Field Measurements," *Journal of Spacecraft and Rockets*, Vol. 41, No. 4, 2004, pp. 490–495.

[20]Kelley, M. C., *The Earth's Ionosphere, Plasma Physics and Electrodynamics*, Academic Press, San Diego, CA, 1989.

[21]Delamere, P. A., Stenbaek-Nielsen, H. C., Pfaff, R. F., Erlandson, R. E., Meng, C. I., Zetzer, J. I., Kiselev, Y., and Gavrilov, B. G., "Dynamics of the Active Plasma Experiment North Star Artificial Plasma Jet," *Journal of Spacecraft and Rockets*, Vol. 41, No. 4, 2004, pp. 503–508.

[22]Gavrilov, B. G., Pdgorny, I. M., Podgorny, I. M., Sobyanin, D. B., Zetzer, J. I., Elrandson, R. E., Meng, C.-I., and Stoyanov, B. J., "Diamagnetic Effect Produced by the Fluxus-1 and 2 Artificial Plasma Jet," *Geophysical Research Letters*, Vol. 26, No. 11, 1999, pp. 1549–1552.

[23]Bruce, C., and Talbot, L., "Cylindrical Electrostatic Probes at Angles of Incidence," *AIAA Journal*, Vol. 13, No. 9, 1985, pp. 1236–1238.

D. L. Cooke
Guest Editor